Article

Tool Run-Out in Micro-Milling: Development of an Analytical Model Based on Cutting Force Signal Analysis

Andrea Abeni [1] , Cristian Cappellini [2] , Greta Seneci [1], Antonio Del Prete [3] and Aldo Attanasio [1,*]

1   Dipartimento di Ingegneria Meccanica ed Industriale, Università degli Studi di Brescia, Via Branze, 38, 25123 Brescia (BS), Italy; andrea.abeni@unibs.it (A.A.); greta.seneci@unibs.it (G.S.)

2   Dipartimento di Ingegneria Gestionale, dell'Informazione e della Produzione, Università degli Studi di Bergamo, Via Pasubio, 7/b, 24044 Dalmine (BG), Italy; cristian.cappellini@unibg.it

3   Dipartimento di Ingegneria dell'Innovazione, Università del Salento, Complesso Ecotekne–edificio "Corpo O", Via per Monteroni, 73100 Lecce (LE), Italy; antonio.delprete@unisalento.it

*   Correspondence: aldo.attanasio@unibs.it; Tel.: +39-030-3715584

Abstract: Micro-machining is a widespread finishing process for fabricating accurate parts as biomedical devices. The continuous effort in reducing the gap between the micro- and macro-domains is connected to the transition from conventional to micro-scale machining. This process generates several undesired issues, which complicate the process's optimization, and tool run-out is one of the most difficult phenomena to experimentally investigate. This work focuses on its analytical description; in particular, a new method to calibrate the model parameters based on cutting force signal elaboration is described. Today, run-out prevision requires time-consuming geometrical measurements, and the main aim of our innovative model is to make the analysis completely free from dimensional measurements. The procedure was tested on data extrapolated from the micro-machining of additively manufactured AlSi10Mg specimens. The strategy appears promising because it is built on a strong mathematical basis, and it may be developed in further studies.

1. Introduction

One of the most thriving areas of industrial research in recent times is the additive manufacturing (AM) of metallic alloys. The AM of metals includes a large collection of different processes, which can be classified by considering how the raw material is supplied (powder or wire or sheet shape) or how the energy is provided (laser, electron beam, or arc) [1]. AM finds several applications in different industries, but biomechanics and aerospace are the sectors where AM is most employed. Light-weight and biocompatible aluminum alloys stand out among processable alloys, and they are also the second most widely used metallic structural material after steel. Aluminum alloys have broad potential for applications in aerospace, automotive, defense, electronics, and biomedical industries, but the performances of parts produced by the traditional casting process are poor [2]. Traditional casting and its low cooling rates cause macro-segregation and coarse structures in aluminum alloys [3]. To overcome this issue, together with the need for a long production chain and the limited flexibility of plastic processing, numerous studies on AM can be found in the literature. In [4], an in-depth analysis of stereolithography (STL) on AlSi10Mg was proposed, while in [5], the same topic was analyzed with a micro-image-based (by X-ray tomography) finite-element simulation, which led to a model for quantifying process-induced defects. The laser-based powder bed fusion (LB-PBF) of AlSi10Mg has been successfully commercialized and has become the most popular additive manufacturing technology for Al alloys owing to its low density and high specific strength [6].

Once an AM complex functional part is produced, it needs further finishing to make the component ready for critical application (aerospace, automotive, biomedical, optical,

military, etc.). This is an example of how different technologies are now combined to exploit their advantages to achieve new properties or uses.

Another important aspect is miniaturization and the high precision requirements of manufacturing processes [7]. Among all of the precision production technologies, micro-milling is one of the most studied because it is promising for accurate feature fabrication. To turn this technology into a large-scale production process, its predictability requires further development. Micro-milling is defined as the result of the scaling down from conventional sizes (feed rates of hundreds of micrometers per tooth, depths of cut equal to several millimeters) to micro-end-milling sizes (feed rates of several micrometers per tooth, depth of cut of hundreds of micrometers) [8], and its accuracy is lower than 1 μm. The integration between AM and micro-machining leads to the definition of hybrid additive manufacturing, which refers to material removal being performed after the 3D fabrication of near-net-shaped products [9]. Micro-machinability at a low dimensional scale is strongly affected by the microstructure and the derived mechanical properties [10] due to the size effect; additively manufactured alloys exhibit specific properties due to the different chemical composition and process conditions, such as localized elevated thermal loads and the consequent high-rate cooling. There is wide literature on the machinability of LB-PBF samples. Owing to the rapid development in hybrid additive manufacturing, reference [11] proposed a comparison between the machinability of cast and LB-PBF samples produced in AlSi10Mg and subjected to T6 solution heat treatment. In [12], another alloy for orthopedic application was investigated to build a numerical model using the DEFORM-3D v11.3 commercial software. The model integrated the experimental cutting parameters and it was used for predicting the formations of serrated chips, chip thickness, and tool wear mechanism. Several studies have been conducted on the final quality of micro-machined parts; in [13,14], surface roughness was investigated and the correlation with the process parameters was discussed.

While traditional milling and micro-milling are equivalent from a kinematic point of view, the main issues connected to the change in sizes are the undesirable phenomena observed at the micro-scale. In the micro-milling of the tool edge radius dimension, the uncut chip thickness and the alloy grain size are of the same order of magnitude, so there is a need to define a new model of the process. In [15], a thorough review about all micro-milling issues, including micro-burr formation mechanisms, cutting temperature, vibrations, surface roughness, cutting fluids, and cutting forces, is available. In particular, the ratio of feed per tooth to the radius of the cutting edge is lower in micro-milling than in conventional machining. The low ratio promotes a negative rake angle, which can cause an incorrect material removal mechanism known as the ploughing condition. Ploughing has negative effects on surface integrity; furthermore, it increases the difficulties in predicting cutting forces. In [15], one of the first numerical attempts to model the effects of temperatures and chip formation on cutting forces during micro-machining operations was performed. In [16], another mechanistic cutting force model was presented, and it considered the effect of high rotational speeds, which amplify tool run-out.

In the cutting force prediction for micro-machining processes, the tool run-out phenomenon plays a primary role. Tool run-out determines the difference between the tool edge's actual and theoretical trajectories [17]. It greatly affects the accuracy of micro-milling, in contrast to conventional milling, where the same phenomenon has neglectable effects. Tool run-out leads to increased tool wear [18] and a reduction in the surface quality for the finished parts [19], and it makes force prediction more difficult. An analytical model for predicting the surface topology when micro-milling three different materials, namely 40HM steel, Al7035 aluminum alloy, and Ti-6Al-4V titanium alloy, was proposed in [20]. The authors revealed that roughness was mainly influenced by the cut width, while a significant effect of the feed was observed only at low cut width values. In [21], a wide description of this topic is presented with a geometrical description; the parameters were the same as those used in this article. The important result in [21] is the experimental method proposed to measure tool run-out from the cutting force signal. Once the mill

diameter, the cutting edge phase angle α, and the rotational radius of the first cutting edge are known, the tool run-out parameters could be estimated. It used the cutting period derived from the cutting force signal to determine α, while for determining the first cutting edge radius the physical measurement of the width of the cut is mandatory. A cutting energy-based model capable of predicting run-out geometry is developed in [22], where good forecasting of machined surface roughness is achieved. In [23], an experimental technique, exploiting the usage of a boring tool holder for evaluating the tool offset modification, is presented. The implementation of a piezo actuator for compensating tool run-out using workpiece displacement improved the accuracy of the machining operation. As all the experimental procedures required to describe the run-out effect are time-consuming, in [24] a valid analytical model to estimate cutting forces is presented; it is applied to a wide range of process parameters, specifically for Inconel samples produced from the AM process. A more complex force predictive model is presented in [25]. It deals with another significant phenomenon in micro-milling: the transition between the ploughing regime and the shearing one. The shearing occurs only when the actual chip thickness increases, and it reaches the minimum uncut chip thickness (*MUCT*). In [26], an analytical model for the evaluation of the asymmetrical behavior of machining forces in micro-milling operations is presented and it considers both the transition between ploughing and shearing regime in cutting and the effects of tool run-out. In [27], the first analytical model for cutting force prediction deals with the transition between the regimes. A tool run-out model based on the replacement of location and tilt tool angle with the tool axis direction vectors, allowing good prediction of instantaneous uncut chip thickness (*IUCT*) and forces, is presented in [28]. In other research [29], a dynamic force model based on the instantaneous stiffness is introduced, permitting the estimation of run-out by calibrating it with the modeled forces. In [30], the aim is not the force prevision, but there is a useful uncut chip thickness model that considers the precise trochoidal trajectory of the cutting edge, tool run-out, and dynamic modulation caused by the machine tool system vibration. Always based on *IUCT*, the effect of tool run-out on the behavior of cutting forces was studied in [31] by flank shearing, ploughing, and bottom edge coefficient calibration. The instantaneous calibration of cutting force coefficients in the presence of tool run-out is also discussed in [32], giving encouraging results.

All the studies previously mentioned are valid for the prediction of cutting forces in micro-milling and they consider the effects of the specific phenomena related to the micro-scale. Nevertheless, the data collection of those methods requires expensive online experimental acquisition devices correlated to direct physical time-consuming offline measurements. Currently, in the literature, there is a lack of models that allow the prevision of run-out from an analytical point of view and without direct measurements on the machined parts. In this work, the force signal directly acquired from micro-milling experiments is used to predict run-out, permitting a future implementation for tool path monitoring and compensation in an online mode. The model reliability is tested by comparing the model results to the experimental ones. It is also mathematically demonstrated that the proposed model applies to different materials. The demonstration was performed with a sensitivity analysis which confirmed the independence of the model from the value of the force-specific constant K_{ts}.

2. Materials and Methods

Tool run-out is a not neglectable phenomenon in the study of the micro-machining process due to the extreme accuracy usually required. For this reason, the modeling of micro-machining must consider the geometrical description of the tool run-out. It allows us to derive some relations between the run-out parameters and to compute a mathematical representation of the process. The model described in this work makes the tool run-out prediction independent from time-consuming experimental measurements: the only variables that it requires are the process geometrical features and the force signals [33,34] automatically recorded during the milling process. The aim of the second part of this section

is the validation of the model so that the extensive experimental campaign is described, and it is used to compare the run-out predicted by the elaboration from the force signal with the actual run-out computed by measuring the machined features.

2.1. Proposed Model

2.1.1. Tool Run-Out

Tool run-out is the result of the sum of many different phenomena, among which are the geometrical displacements of the spindle axis, tool-holder axis, and tool axis from the theoretical rotation axis.

Figure 1 represents the run-out effect on the tool together with the geometric main parameters which must be considered in the discussion [21]. The two tool-cutting edges are sectioned in a plane normal to the theoretical tool rotation axis and parallel to the feed direction.
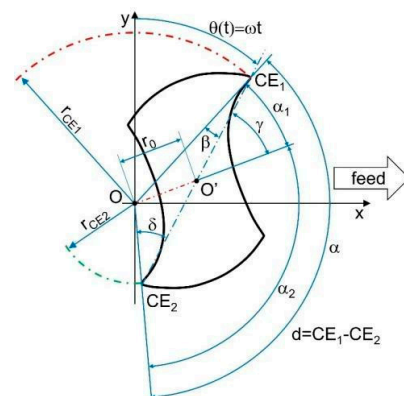

Figure 1. Geometrical representation of tool run-out.

The two main run-out parameters are:

- r_0, the distance between the spindle's rotational center O and the tool one O';
- γ_0, the angle from r_{ce1} and r_0.

They cannot be experimentally measured, but there are mathematical equations to compute them from other geometrical variables (Equations (1)–(4)). Those equations are widely discussed in Attanasio's work [21]:

$$r_{CE1} = \underline{OA} = \left(\frac{d}{2} + r_0\right)\cdot\sqrt{1 + \frac{d\cdot r_0\cdot(cos\gamma - 1)}{\left(\frac{d}{2} + r_0\right)^2}} \tag{1}$$

$$r_{CE2} = \sqrt{r_{CE1}^2 + d^2 - 2r_{CE1}\cdot d\beta} \tag{2}$$

$$\delta = arcsin\left(\frac{\underline{OA}}{\underline{AB}}\cdot sin\,\alpha\right) \tag{3}$$

$$\beta = \pi - \alpha - \delta \tag{4}$$

The variables included in the previous equations are:

- the tool diameter d [mm];
- the rotational speed ω [rad/s];
- the cutting edge phase angle α [rad].

The only term that is required to be experimentally found for its use in the final equation is r_{CE1} [mm], the rotational radius of the main cutting edge. The tool run-out causes the variation of two parameters previously described:

1. angle α would not be constantly equal to π [rad];

2. radius r_{CE1} would differ from the rotational radius of the second cutting edge r_{CE2} [mm].

2.1.2. Analytical Model

In [21], further equations are presented to compute all the geometrical quantities visible in Figure 1. In [21], there are also the equations to describe the cutting trajectories of the two tool edges (Equations (5)–(9)). The term called $\theta(t)$ is the tool rotational angle which is a function of time (Equation (5)). In the following equation, *CE*1 stands for the first cutting edge while the subscript *CE*2 is used to refer to the second cutting edge.

$$\theta(t) = \omega \cdot t \tag{5}$$

$$x_{CE1} = r_{CE1} \cdot sin\ \theta + \frac{f}{60} \cdot t \tag{6}$$

$$y_{CE1} = r_{CE1} \cdot cos\ \theta \tag{7}$$

$$x_{CE2} = r_{CE2} \cdot sin\ [\theta + \alpha] + \frac{f}{60} \cdot t \tag{8}$$

$$y_{CE2} = r_{CE2} \cdot cos\ [\theta + \alpha] \tag{9}$$

In [26], the previous equations are derived to estimate the instantaneous uncut chip thickness (*IUCT*) (Equations (10)–(13)). Each one of the two mill cutting edges has its value for *IUCT* and they are called h_{CE1} and h_{CE2} (Figure 2a). In the following functions, Δs_{CE1} is the distance crossed by the rotational axis between the passage of the second cutting edge *CE*2 and the consecutive passage of the first one, *CE*1, in the θ instantaneous angular position; vice versa, the value Δs_{CE2} is the distance defined from the passage of the rotational axis of *CE*1 and the consecutive passage of the one for *CE*2, always in the θ angular position.

$$h_{CE1} = \sqrt{(r_{CE1}sin\ \theta + \Delta s_{CE1})^2 + (r_{CE1}cos\ \theta\ )^2} - r_{CE2} \tag{10}$$

$$h_{CE2} = \sqrt{(r_{CE2}sin\ \theta + \Delta s_{CE2})^2 + (r_{CE2}cos\ \theta\ )^2} - r_{CE1} \tag{11}$$

$$\Delta s_{CE1} = \frac{f}{60} \cdot \frac{\alpha}{\omega} \tag{12}$$

$$\Delta s_{CE2} = \frac{f}{60} \cdot \frac{2\pi - \alpha}{\omega} \tag{13}$$

Then, the cutting area of the i-th cutting edge is determined (Equation (14)) to be used later in the calculation of ploughing areas; indeed, two of the variables in the cutting force equation are the ploughing areas and not the overall cutting area.

$$A_{ci}(\theta) = \int_0^\theta \left(\frac{h_{CEi}(\theta) + h_{CEi}(\theta + d\theta)}{2} \right) \cdot r_{CEi} \cdot d\theta \tag{14}$$

While the cutting area A_{ci} is the total surface of material removed by a single cutting tool edge, Ap_{CE1} and Ap_{CE2} are defined as the ploughed area for the two cutting edges [mm^2] (see Figure 2a). The ploughed area is the portion of the cutting area where the material is deformed and not cut. The so-called minimum uncut chip thickness (*MUCT*) must be used to detect the transition from the ploughing regime to the shearing one. As Equations (15)–(17) show [25], when *MUCT* is higher than $h_{CEi}(\theta)$ the cutting area of the i-th edge is equal to the ploughing one. From Equation (16), it is possible to state that when *MUCT* is lower than the $h_{CEi}(\theta)$ value, the i-th cutting edge's ploughing area (A_{pCEi}) is equal to the maximum one among all the cutting edges (A_{pMAX}). Another result is that if

the value of *MUCT* is lower than $h_{CEi}(90°)$, the cutting area for the edge is the maximum possible and it is equal to the ploughing area.

$$h_{CEi}(\theta) < MUCT \bigwedge \theta < \theta_{MAXi} \rightarrow A_{pCEi}(\theta) = A_{ci}(\theta) \tag{15}$$

$$hCEi(\theta) > MUCT \rightarrow A_{pi}(\theta) = A_{piMAX} \tag{16}$$

$$h_{CEi}(\theta) < MUCT \bigwedge \theta > \theta_{MAXo} \rightarrow A_{pCEi}(\theta) = A_{ci}(\pi) - A_{ci}(\theta) \tag{17}$$

The total cutting force F_c is the combination of its axial components F_x, F_y, and F_z in the three dimensions. In Figure 2a, the F_z component is not visible because it is orthogonal to the section plane. The resulting F_c could also be subdivided into its tangential F_t and radial F_r components; the tangential direction follows the cutting edge θ generic angular position and it is defined in a plane orthogonal to the tool axis. These last force components can be expressed by Equations (18)–(21) for the two cutting edges:

$$F_{t1} = \left(K_{ts} \cdot h_{CE1}(\theta) + K_{tp} \cdot A_{pCE1}(\theta)\right) \cdot a_p \tag{18}$$
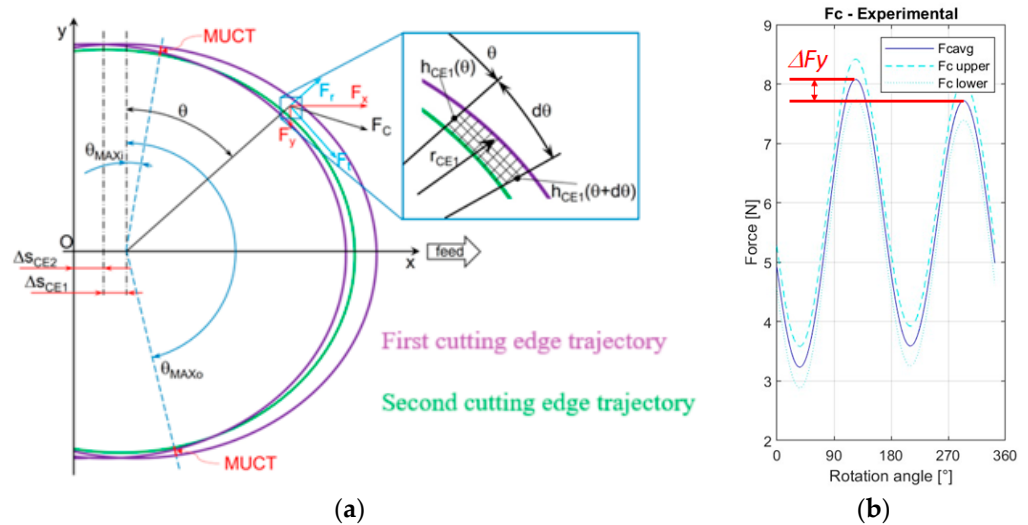
$$F_{r1} = \left(K_{rs} \cdot h_{CE1}(\theta) + K_{rp} \cdot A_{pCE1}(\theta)\right) \cdot a_p \tag{19}$$

$$F_{t2} = \left(K_{ts} \cdot h_{CE2}(\theta) + K_{tp} \cdot A_{pCE2}(\theta)\right) \cdot a_p \tag{20}$$

$$F_{r2} = \left(K_{rs} \cdot h_{CE2}(\theta) + K_{rp} \cdot A_{pCE2}(\theta)\right) \cdot a_p \tag{21}$$

where:

- a_p is the axial depth of cut [mm];
- K_{ts} and K_{rs} are the specific force coefficients for the shearing regime [N/mm^2];
- K_{tp} and K_{rp} are the specific force coefficients for the ploughing regime [N/mm^3].

Figure 2. Cutting forces in micro-milling: (**a**) Cutting edge trajectories, instantaneous uncut chip thickness (IUCT) ($h_{CEi}(\theta)$), minimum uncut chip thickness (MUCT), and force components represented on the plane orthogonal to tool axial axis; (**b**) Trend of total cutting force (F_c) vs. tool rotational angle (θ).

Once the force tangential and radial components are determined, in Equations (22)–(25) there is the mathematical passage to the force components for the *x*-axis and *y*-axis.

$$F_{x1} = F_{t1} \cdot cos\,\theta + F_{r1} \cdot sin\,\theta \tag{22}$$

$$F_{y1} = -F_{t1} \cdot sin\,\theta + F_{r1} \cdot cos\,\theta \tag{23}$$

$$F_{x2} = F_{t2} \cdot cos\,\theta + F_{r2} \cdot sin\,\theta \tag{24}$$

$$F_{y2} = -F_{t2} \cdot sin\ \theta + F_{r2} \cdot cos\ \theta \tag{25}$$

Considering that the peak force of the two cutting edges will be in correspondence with maximum chip cross-sectional area, for *CE1* the peak will be when $\theta \cong 90°$ while for CE2 the peak will be when $\theta \cong 270°$ (Figure 2b). Introducing those values in Equations (22)–(25) and using the definitions for the force components in Equations (18)–(21), a new function (Equation (26)) is found to define the peak difference for the y component (it is ΔF_y in Figure 2b); the y-axis is orthogonal to the feed direction.

$$\frac{\Delta Fy(90°)}{a_p} = K_{ts}(h_{CE1}(90°) - h_{CE2}(90°)) + K_{tp}(A_{pCE1}(90°) - A_{pCE2}(90°)) \tag{26}$$

The following hypothesis is assumed: the ploughing areas for the two cutting edges could be considered equal. This statement is consequential of the use of a high-precision tool holder which will determine a small value of run-out; a small run-out is the result of cutting edge trajectories being very similar (r_{CE1} equal to r_{CE2} and Δs_{CE1} equal to Δs_{CE2}), so the ploughing areas will be the same. Equations (15)–(17) exploit that if $h_{CE1}(90°)$ is higher than *MUCT*, the ploughing area of the first cutting edge is equal to the maximum ploughing area among all the tool cutting edges; in the study case, the cutting edges are only two, so $A_{pCE1}(\theta)$ is equal to $A_{pCE2}(\theta)$. The hypothesis that $A_{pCE1}(\theta)$ is equal to $A_{pCE2}(\theta)$ allows us to simplify Equation (26) by writing Equation (27):

$$\frac{\Delta Fy(90°)}{a_p} = K_{ts}(h_{CE1}(90°) - h_{CE2}(90°)) \tag{27}$$

In the passage from Equation (26) to Equation (27), all the specific force coefficients previously presented can be neglected except for K_{ts}; its definition needs a sensitivity analysis to investigate its effect on the final analytical equation.

As the θ value is fixed, the variable ΔF_y becomes independent from the angular position and an angle of 90° leads to the maximum of the y component peak difference (ΔF_{ymax}). At the same time, when θ reaches the value of 90°, the functions to find h_{CE1} and h_{CE2} can be rewritten and Equation (28) is determined.

$$\frac{\Delta Fymax}{K_{ts} \cdot a_p} = 2 \cdot (r_{CE1} - r_{CE2}) + \Delta s_{CE1} - \Delta s_{CE2} \tag{28}$$

By applying the definitions of Δs_{CE1} and Δs_{CE2} presented in Equations (12) and (13), Equation (28) can be simplified in Equation (29):

$$r_{CE1} - r_{CE2} = I = \frac{\Delta Fymax}{2 \cdot K_{ts} \cdot a_p} - \frac{f}{60 \cdot \omega}(\alpha - \pi) \tag{29}$$

The difference between the two cutting radii will be called in all the further equations variable *I*. Variable ΔF_{yMAX} can be estimated by the analysis of the cutting force signal. Substituting in Equation (29) the values of r_{CE2} and β, the final 4th grade equation to estimate r_{CE1} is found (Equation (30)). All the variables written in the model are described in Equations (31)–(35).

$$a \cdot r_{CE1}{}^4 + b \cdot r_{CE1}{}^3 + c \cdot r_{CE1}{}^2 + e \cdot r_{CE1} + g = 0 \tag{30}$$

$$a = sin^4(\alpha) + cos^2(\alpha) \cdot sin^2(\alpha) \tag{31}$$

$$b = -2 \cdot I \cdot sin^2(\alpha) \tag{32}$$

$$c = I^2 + I^2 \cdot sin^2(\alpha) - d^2 \cdot sin^2(\alpha) - d^2 \cdot cos^2(\alpha) \tag{33}$$

$$e = I \cdot d^2 - I^3 \tag{34}$$

$$g = \left(\frac{l^2}{2} - \frac{d^2}{2} \right)^2 \qquad (35)$$

Equation (30) allows us to compute r_{CE1} and, once it is known, the geometrical model of tool run-out is defined. The previous approach described in [26] required the experimental determination of r_{CE1} by measuring the width of the microchannels and by assuming that the width is equal to double r_{CE1}. In this work, both methodologies were applied to compare the results to validate the innovative approach. In the case that the experimental results would be coherent with the values predicted by Equation (30), the hypothesis on which the innovative approach is based can be considered valid.

2.2. Experimental Campaign

The experimental campaign consists of micro-milling of slots in AlSi10Mg alloy specimens fabricated via LB-PBF. In Table 1, there is the chemical composition of the alloy.

Table 1. Chemical composition of AlSi10Mg (weight percentage).

| AlSi10Mg	Si	Fe	Mn	Mg	Cu	Al
LB-PBF	10.2	0.21	<0.02	0.40	<0.002	Balance

2.2.1. Specimen Preparation

The prismatic specimen used in the tests was built through laser-based powder bed fusion (LB-PBF). The additive machine used for the specimen production is an EOS M290 (EOS GmbH, Krailing, Germany) and in Table 2 the process parameters are listed. The specimen was also subjected to two further treatments: hot isostatic pressing (HIP) followed by T6 heat treatment. The HIP mechano-thermal treatment consists of heating to 520 °C for 2 h while the T6 heat treatment consists of a solution treatment at 540 °C for 7 h, followed by quenching in water and artificial aging at 160 °C for 4 h.

Table 2. LB-PBF process parameters.

Parameter	Value
Laser power [W]	370
Scanning speed [mm/s]	1300
Hatching distance [μm]	190
Layer thickness [μm]	30
Building platform temperature [°C]	80
Scanning direction	Vertical (z)

The sample shape was designed to constrain the sample itself on the load cell; so, two small holes have been made at the specimen edges (see Figure 3). The surface roughness was measured by using a laser profilometer (Mitaka PF60, Mitaka Kohki Co., Ltd., Tokyo, Japan) by repeating three measurements. It resulted in Ra = 16.9 ± 4.1 μm and Rz = 89.9 ± 21.4 μm.

(**a**)　　　　　　　　　　　　　　　　　　　　　　　(**b**)
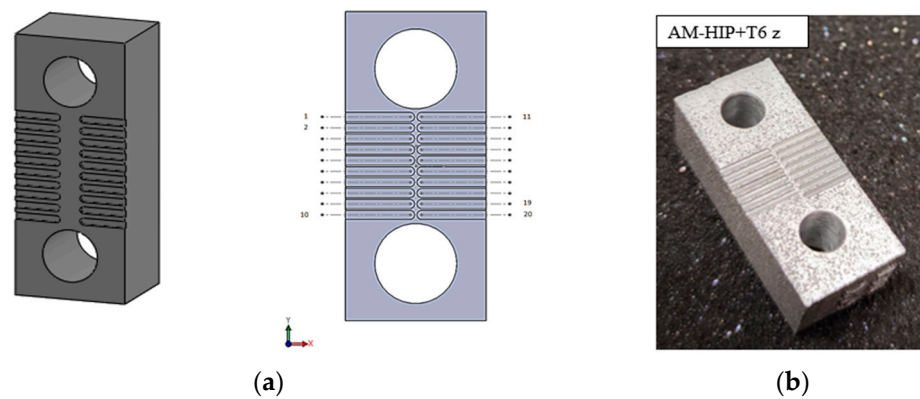
Figure 3. The AM specimen with the micro-channels made from micro-milling: (**a**) sample 3D drawing and the micro-slot scheme; (**b**) photo of the real specimen.

2.2.2. Micro-Milling Experiments

The tool used in the micro-milling experiments is a Ø0.8 mm flat-bottom two-flute micro-mill. In Table 3, there are the main features of the tool. The tool diameter was measured three times before every milling test and by using a multifocal microscope (Hirox RH-2000, Hirox Japan Co., Ltd., Tokyo, Japan).

Table 3. Properties of the tool employed for the micro-slot machining.

Property	Value
Model	103L008R005-MEGA-64-T
Nominal diameter [μm]	800
Effective diameter [μm]	789 ± 2
Nom. tool corner radius [μm]	5
Eff. tool corner radius [μm]	6.3
Helix angle [°]	20°
Rake angle [°]	4°
Material	Tungsten carbide
Coating material	Titanium nitride

In Figure 3, there is a representation of the micro-slot scheme. As Figure 3b shows, 15 micro-slots have been fabricated during the milling experiments on the AM specimen. In the pattern of Figure 3b, it is possible to see 20 slots because excess space was designed to have the possibility to repeat tests in cases of issues about the cutting force data acquirement. The cutting parameters used in the milling tests are listed in Table 4. Fourteen values of feed per tooth f_z were tested, by ranging the parameters between 0.5 μm/tooth and 7 μm/tooth with an increment of 0.5 μm/tooth between two consecutive tests. Feed per tooth is the parameter that determines the chip cross-section and consequentially its values have been chosen to investigate both the ploughing cutting regime and the shearing regime and the transition among them to extend the validation of the innovative procedure.

Table 4. Cutting parameters.

Parameter	Value
Cutting speed v_c [m/min]	80
Axial depth a_p [mm]	0.25
Feed per tooth f_z [μm/tooth]	0.5–7.0

The micro-milling tests were performed on a five-axis Nano Precision Machining Centre (KERN Pyramid Nano, Kern Microtechnik GmbH, Eschenlohe, Germany) equipped with a Heidenhain iTCN 530 numeric control. The experimental tests were performed on

the as-built surface achieved by the LB-PBF process. The load cell was a Kistler 9317C (Kistler Instrumente AG, Winterthur, Suisse), a piezoelectric 3-component force sensor, interfaced to three charge amplifiers (Kistler 5015A, Kistler Instrumente AG, Winterthur, Suisse). The force-measuring system accuracy is equal to 0.1 N and the sampling rate is 20 kHz. The natural frequency (2145 Hz for F_x and 2192 Hz for F_y as characterized in [35]) is lower than the tooth path frequency. The sample is fixed to the load cell with two screws. From the signal, a portion corresponding to thirty tool rotations was extrapolated to calculate the average cutting force signal. The optical measurement instrument used to determine micro-channels widths and depths was a Mitaka PF60 laser profilometer probe and in Table 5 its main properties are presented.

Table 5. Laser profilometer properties.

Property	Value
Range measurement [mm]	$60 \times 60 \times 10$
x, y resolution [μm]	0.1
z resolution [μm]	0.01
Laser spot diameter [μm]	1
Laser wavelength [nm]	635

2.2.3. Tool Run-Out Measurement

The micro-slot theoretical width is approximated to be twice the r_{CE1} value (Figure 4a). The laser-scanning speed used in the experimental measure was 20 μm/s and the measuring software was MountainsMap® Premium version by Digital Surf. As Figure 4b and c show, each of the measures presented in the Results section is the result of the mean of different measures. Considering that the mean micro-slot length is equal to 4500 μm, every micro-slot width measured is the mean of five measures that have been made every 1125 μm (Figure 4b). At the same time, the depth of the channels has been estimated from the mean of 3 measurements taken every 2250 μm of the specimen length (Figure 4c). The mechanical deburring was performed on the specimen before the width measurement while the depth measures were made from the original specimen to avoid measure falsification.


| (a) | (b) | (c) |
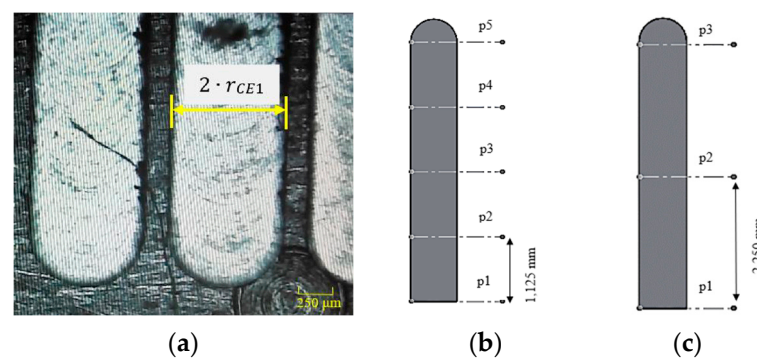
Figure 4. Experimental measures on the specimen: (**a**) value of r_{CE1} derived from the micro-slot width; (**b**) width measure acquisition scheme; (**c**) depth measure acquisition scheme.

Dealing with the cutting force signal, a Matlab script was elaborated to detect the difference between the two cutting force peaks in the y-direction. As highlighted in Figure 1, the phase angles of the two cutting edges are not constant and equal to π. Referring again to Figure 1, the *CE*1 phase angle is equal to the difference between the full angle (2π) and the phase angle α of *CE*2. This implicates different cutting times for *CE*1 and *CE*2, defined as T_1 and T_2, respectively. Considering the behavior of the theoretical cutting force component F_y during the total cutting period T (the time which is spent by the tool to complete one full rotation), reported in Figure 5, T_1 and T_2 can be measured as the time difference between the two sequential valleys of the force signal. As a consequence, applying the equations

presented in [21], the phase angles of *CE*1 and *CE*2 can be determined as fractions of the full angle. In particular, α is the full angle fraction related to the period fraction T_2, as reported in Equation (36). Figure 5 also depicts the difference between the peaks of the two cutting edge forces ΔF_y.

$$\alpha = 2\pi \cdot \frac{T_2}{T} \tag{36}$$
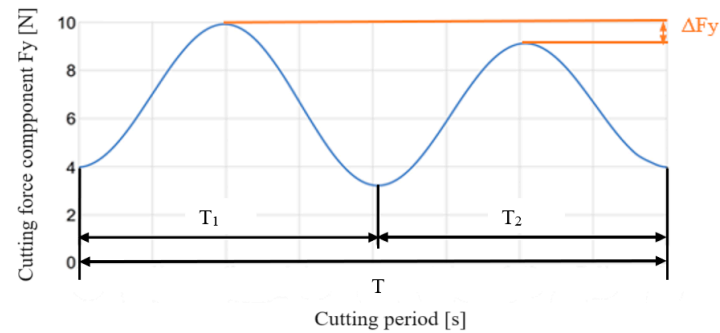
Figure 5. Theoretical cutting force signal as a function of time.

3. Results and Discussion

In this section, the experimental results are presented together with the calculation of the run-out parameters by using both the theoretical equation and the experimental measurements. In the next subsection, the described analytical model is applied to the study case while a comparison between experimental values and analytical ones is proposed afterwards. In the last part of this section, a simplification of Equation (30) from a 4th grade equation to a 2nd grade model is derived from mathematical consideration and approximations.

3.1. Experimental Measures

In Table 6, the width and depth measures of micro-slots are presented. The tool diameter was always measured before the execution of the tests and it was observed that the diameter was equal to 789 ± 2 μm. An ideal milling process generates a micro-slot width equal to twice the tool effective radius and a micro-slot width measure of 0.789 mm reflects a lack of run-out effect. Consequentially, the presence of run-out can be found where the width measure is higher than the ideal value just introduced. However, none of the measures has been discarded because they are also affected by the presence of burrs; a micro-slot width lower than 0.787 mm (which is exactly the minimal value of the tool's effective diameter) means that the laser profilometer measured the distance between two irregular surfaces covered by burrs. In Figure 6, there is one of the images of the micro-slots after deburring, obtained by the multifocal 3D optical microscope.
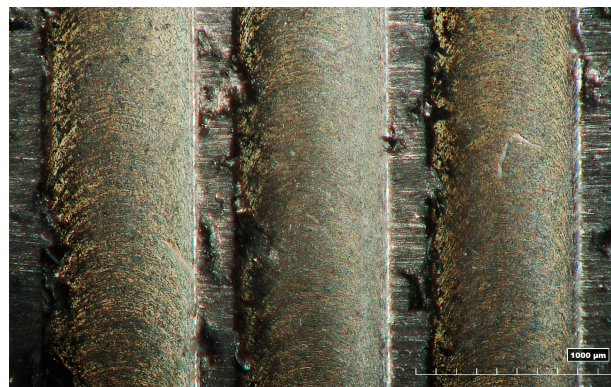

Figure 6. Micro-slot image obtained from the microscope after deburring.

Table 6. Measures of micro-slots machined on AM-HIP+T6 z specimen.

Test	f_z [mm/tooth]	f [mm/min]	Average Width [mm]	Dev St Width [mm]	Average a_p [mm]	Dev St a_p [mm]	Experimental r_{CE1} [mm]
1	0.0010	64	0.7604	0.0219	0.2607	0.0297	0.3802
2	0.0045	286	0.7755	0.0073	0.2373	0.0317	0.3878
3	0.0020	127	0.7816	0.0066	0.2385	0.0204	0.3908
4	0.0060	382	0.7816	0.0035	0.2502	0.0167	0.3908
5	0.0025	159	0.7662	0.0058	0.2391	0.0192	0.3831
6	0.0040	255	0.7792	0.0130	0.2374	0.0100	0.3896
7	0.0015	95	0.7730	0.0135	0.2545	0.0154	0.3865
8	0.0030	191	0.7960	0.0242	0.2590	0.0172	0.3980
9	0.0035	223	0.7896	0.0174	0.2616	0.0173	0.3948
10	0.0005	32	0.7879	0.0171	0.2641	0.0074	0.3940
11	0.0065	414	0.8021	0.0055	0.2676	0.0140	0.4010
12	0.0055	350	0.7829	0.0234	0.2541	0.0072	0.3915
13	0.0050	318	0.7951	0.0198	0.3119	0.0061	0.3975
14	0.0070	446	0.7997	0.0272	0.2477	0.0167	0.3998

From the average width values, it could be observed that the variation of the feed per tooth values used in the tests has a neglectable effect on the measures; the difference between r_{CE1} maximum and minimum values is lower than 0.02 mm. Furthermore, in the literature [24,26], the value of feed per tooth considered as the limit in the transition from the ploughing regime to shearing is between 1.5 μm/tooth and 2 μm/tooth. From these statements, it could be said that the conclusion of the method presented will be associated with both regimes. Analyzing the measures presented in the previous table, it could be seen that eight of the fifteen micro-slot average width measures are lower than 0.787 mm.

Following that, the Matlab script was applied to the cutting force data to estimate the differences between force peaks in the y-direction. Equation (36) was used to compute the α for each micro-machining test. The results are collected in Table A1, reported in Appendix A, while the graphical representation of phase angles with respect to the peak force differences with their standard deviations is depicted in Figure 7. From a theoretical point of view, the test more affected by tool run-out is the one with the higher ΔF_y peak and r_0 peak while the value of the α angle is the lowest (it means it will be more different from the ideal 180°). From Figure 7, it can be observed that the test with f_Z equal to 3.0 μm (number 8) is the one where there are the maximum ΔF_y and the minimum α. Moreover, the tendency of α to reach the ideal value of 180° while decreasing ΔF_y is visible as well, as expected by theoretical considerations.
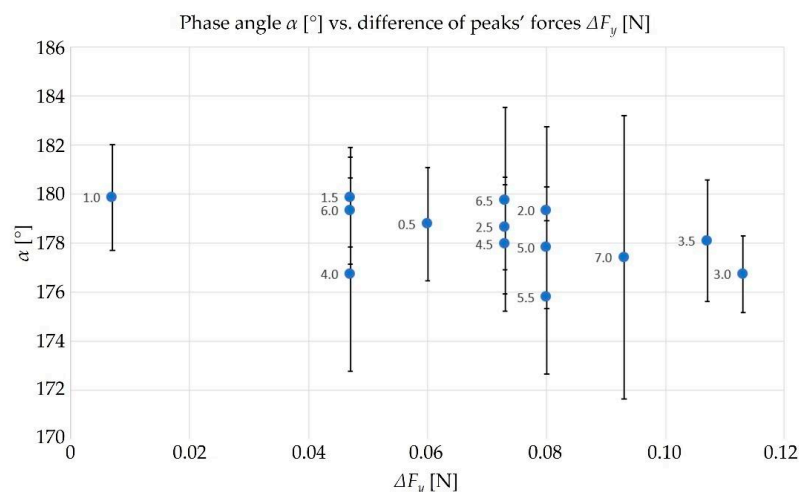
Figure 7. Experimental values of α, and related standard deviation, as a function of ΔF_y. For each test, represented by a dot, the correspondent value of f_Z is reported.

The run-out parameters have been calculated from Equations (1)–(4) by using the experimental value for r_{CE1}, d, and α. In Table 7, there are the main tool run-out parameters (r_0 and γ) calculated from the tests.

Table 7. Run-out parameters computed with the experimental r_{CE1}.

Test	f_z [mm/tooth]	r_0 [mm]	γ [rad]
1	0.0010	0.014	0.032
2	0.0045	0.010	0.803
3	0.0020	0.004	0.552
4	0.0060	0.004	0.557
5	0.0025	0.012	0.385
6	0.0040	0.012	1.149
7	0.0015	0.008	0.057
8	0.0030	0.012	1.281
9	0.0035	0.007	1.535
10	0.0005	0.004	1.440
11	0.0065	0.007	0.136
12	0.0055	0.015	1.346
13	0.0050	0.008	1.195
14	0.0070	0.010	1.038

3.2. Application of the Analytical Model

The implementation of the model (Equation (30)) needs the calibration of the K_{ts} variable for the AlSi10Mg alloy before the calculation of r_{CE1} values. Therefore, to evaluate the influence of K_{ts} value on the model constants in Equation (30), a sensitivity analysis of K_{ts}, in a range from 1 to 10^6 N/mm^2, has been performed. The results are reported in Table A2 where the first outcome is that the terms which assume the highest value are g and $c \cdot (r_{CE1})^2$. In the literature, common values of K_{ts} for metallic alloys are higher than 10^3 N/mm^2 and it can be supposed that AlSi10Mg has analogue K_{ts}. Assuming this hypothesis ($K_{ts} > 10^3$ N/mm^2), the order of magnitude of g and $c \cdot (r_{CE1})^2$ is 10^{-2}, while the other terms range between 10^{-5} and 10^{-8}. The analysis also shows how higher values of K_{ts} lead to lower values for the Equation (30) terms, as the influence of K_{ts} on the model variables is reduced. In conclusion, the terms $a \cdot (r_{CE1})^4$, $b \cdot (r_{CE1})^3$, and $e \cdot (r_{CE1})$ are approximated to zero.

In Figure 8, the non-neglectable terms of Equation (30) are plotted as a function of K_{ts}. In further calculations, a value of 10,000 N/mm^2 is used for K_{ts} as it is clear from Figure 8 that K_{ts} values higher than 10 N/mm^2 do not affect Equation (30).

(a)

(b)
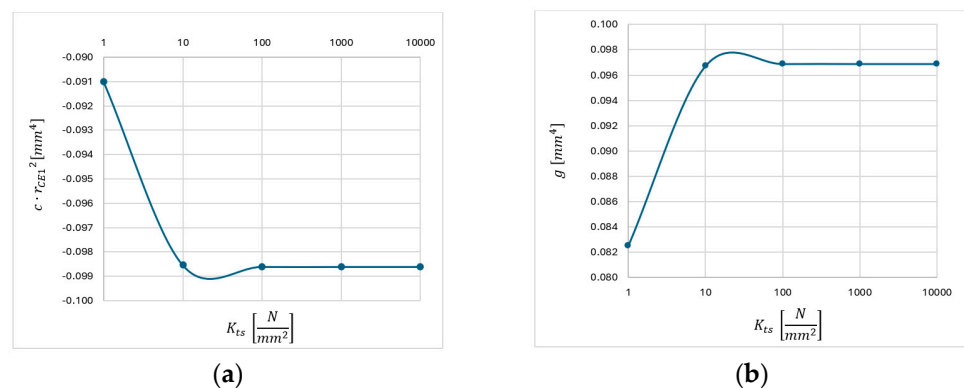
Figure 8. Trends of (**a**) variable g; (**b**) factor $c \cdot (r_{CE1})^2$ as a function of K_{ts}.

3.3. Comparison between the Results

For estimating the analytical value of r_{CE1}, the parameters of Equation (30) have been calculated for each experimental test. Equation (29) has been applied for the calculation of I with a value of K_{ts} equal to 10,000 N/mm^2. For completeness, all the terms are reported in

Table A3. The parameters *a*, *b*, *c*, *e*, and *g* have been determined from *I* and used together with experimentally measured *d*, *α*, ΔF_y, a_p parameters to solve the 4th grade equation. The solving algorithm applied to find the analytical values for r_{CE1} is the Lin–Bairstow method; the results are presented in Table 8, where there is also a comparison between r_{CE1} experimental values and the ones analytically computed. For each test, the Δ *variation* is the difference between the analytical r_{CE1} values and the experimental ones while the percentage error is the Δ *variation* divided by the analytical r_{CE1}.

Table 8. Comparison between experimental and computed r_{CE1} values for each experimental test.

Test	fz [mm]	Experimental r_{CE1} [mm]	Analytical r_{CE1} [mm]	Δ Variation [mm]	Percentage Error [%]
1	0.0010	0.38018	0.39450	0.01432	3.63%
2	0.0045	0.38777	0.39460	0.00683	1.73%
3	0.0020	0.39082	0.39452	0.00370	0.94%
4	0.0060	0.39078	0.39452	0.00374	0.95%
5	0.0025	0.38308	0.39454	0.01146	2.91%
6	0.0040	0.38961	0.39470	0.00509	1.29%
7	0.0015	0.38651	0.39451	0.00799	2.03%
8	0.0030	0.39800	0.39470	−0.00330	−0.84%
9	0.0035	0.39479	0.39458	−0.00021	−0.05%
10	0.0005	0.39397	0.39453	0.00056	0.14%
11	0.0065	0.40104	0.39451	−0.00653	−1.65%
12	0.0055	0.39145	0.39484	0.00339	0.86%
13	0.0050	0.39754	0.39461	−0.00293	−0.74%
14	0.0070	0.39983	0.39466	−0.00517	−1.31%

As shown in Table 8, and considering the first three decimals, the value of r_{CE1} calculated in all the experimental tests is the same and it is close to half the theoretical tool diameter (0.3945 mm).

3.4. Simplification of the Model

The sensitivity analysis demonstrates that only two parts of Equation (30) could not be approximated to zero. In Equation (37), Equation (30) is proposed without the null constants *a*, *b*, and *e*.

$$c \cdot r_{CE1}^2 + g = 0 \tag{37}$$

This 2nd grade equation leads to a simplified equation to predict r_{CE1}:

$$r_{CE1} = \pm\sqrt{-\frac{g}{c}} \tag{38}$$

From Table A2, it could be observed that the values for *g* and $c \cdot (r_{CE1})^2$ are nearly the same between all tests; it demonstrates why the model results are not heavily affected by the variation of the feed per tooth. In Table 9, there is a comparison between the r_{CE1} values calculated from the complete 4th grade equation and the ones from the simplified 2nd grade model. As is shown, the difference between the two equations is always lower than 0.07% so the simplified version of the analytical method could be considered valid.

Table 9. Comparison between the analytical r$_{CE1}$ values calculated from the 4th grade and the 2nd grade equations, for each experimental test.

Test	fz [mm]	4th Grade r$_{CE1}$ [mm]	2nd Grade r$_{CE1}$ [mm]	Δ Variation %
1	0.0010	0.39450	0.39450	0.00007%
2	0.0045	0.39460	0.39453	0.01591%
3	0.0020	0.39452	0.39451	0.00166%
4	0.0060	0.39452	0.39452	0.00173%
5	0.0025	0.39454	0.39452	0.00694%
6	0.0040	0.39470	0.39454	0.04082%
7	0.0015	0.39451	0.39451	0.00007%
8	0.0030	0.39470	0.39454	0.04046%
9	0.0035	0.39458	0.39453	0.01384%
10	0.0005	0.39453	0.39451	0.00568%
11	0.0065	0.39451	0.39451	0.00026%
12	0.0055	0.39484	0.39457	0.06759%
13	0.0050	0.39461	0.39454	0.01814%
14	0.0070	0.39466	0.39456	0.02531%

Moreover, Table 9 reveals that both the formulations of the analytical model (4th grade and 2nd grade equations) lead to the calculation of r_{CE1} values nearly identical to half the tool diameter, regardless of the cutting condition. This result does not agree with the reality, because that condition reflects the lack of tool run-out effect in every test while the experimental measures of r_{CE1} in Table 6 depend on the process parameters. For this reason, it has been proved that the analytical model elaborated is not effective in tool run-out calculation.

4. Conclusions

In this work, a methodology for evaluating the tool run-out based on the peak force difference between the first and second cutting edge in micro-milling is presented. Starting from a mechanistic model of micro-milling forces, already validated in previous research, 4th and simplified 2nd grade equations in the first cutting edge radius (r_{CE1}) domain have been derived. The solution of these equations gives the value of r_{CE1}, necessary for the calculation of tool run-out parameters. Being able to derive both r_{CE1} and the cutting edge phase angle directly from force measurements should give the possibility of instantaneously estimating the amount of tool run-out. This could allow future online run-out monitoring and compensation.

However, the solutions of the proposed equations are not in accordance with the experimental r_{CE1} results, giving values close to micro-mill radius that differ by only tens of microns. The consequence of this finding is that an experimental procedure for the measure of micro-slots is still required in the study of the tool run-out effect in milling. It has also been proved that the experimental measure is badly affected by the presence of burrs; in fact, more than half of the experimental width measures were lower than the tool diameter. According to this, further developments of the analytical method for the prediction of run-out become more necessary.

The reasons for the model incorrectness could be found in the use of a well-performing cutting tool and micro-milling machine. In good working conditions, the tool run-out effect will be weak so it becomes more difficult its study and measure it. Even if accurate instruments have been used, their resolutions could be a problem: the laser profilometer resolution in the plane (0.1 μm) is exactly equal to the first changing decimal in the analytical r_{CE1} values as the force-measuring system accuracy is equal to 0.01 N that is the first changing decimal in ΔF_y values calculated.

The study of more critical cutting conditions could lead to better results. Further studies could test cutting tools affected by severe wear and fixed to the spindle with a less accurate tool holder. In these conditions, the run-out effect is prominent so that it

will be easily detectable in experiments. This case of study will require a completely different analytical model because the one presented in the research is based on the strong hypothesis of equal ploughing areas between the two cutting edges. This statement is justified when the cutting tool works in ideal conditions, but it is not applicable in harder cutting conditions.

In future research, the validity of further analytical models could be proved without any time-consuming experimental test but by the generation of a dataset for the ΔF_y values. This will avoid the inclusion of the effect of the presence of burrs on the micro-slot width measures.

Author Contributions: Conceptualization, C.C., A.A. (Andrea Abeni) and A.A. (Aldo Attanasio); methodology, C.C., A.A. (Andrea Abeni) and A.A. (Aldo Attanasio); software, A.A. (Andrea Abeni); validation, G.S., C.C., A.A. (Andrea Abeni), A.D.P. and A.A. (Aldo Attanasio); formal analysis, C.C.; investigation, A.A. (Andrea Abeni); data curation, G.S. and A.A. (Andrea Abeni); writing—original draft preparation, G.S.; writing—review and editing C.C., A.A. (Andrea Abeni), A.D.P. and A.A. (Aldo Attanasio); supervision, A.A. (Aldo Attanasio). All authors have read and agreed to the published version of the manuscript.

Data Availability Statement: The data that support the findings of this study are not openly available due to reasons of sensitivity and are available from the corresponding author upon reasonable request. Data are located in controlled access data storage at the University of Brescia.

Conflicts of Interest: The authors declare no conflicts of interest.

Appendix A

The appendix reports additional numerical information in the form of tables.

Table A1. Force signal referring to AM-HIP+T6 z machining tests.

Test	f_z [mm/tooth]	ΔFy [N]	α [°]	Dev St α [°]	α [rad]
1	0.0010	0.007	179.87	2.16	3.14
2	0.0045	0.073	177.96	2.74	3.11
3	0.0020	0.080	179.34	3.40	3.13
4	0.0060	0.047	179.33	2.19	3.13
5	0.0025	0.073	178.65	1.74	3.12
6	0.0040	0.047	176.73	3.95	3.08
7	0.0015	0.047	179.87	2.03	3.14
8	0.0030	0.113	176.74	1.56	3.08
9	0.0035	0.107	178.09	2.48	3.11
10	0.0005	0.060	178.78	2.32	3.12
11	0.0065	0.073	179.74	3.81	3.14
12	0.0055	0.080	175.79	3.12	3.07
13	0.0050	0.080	177.82	2.49	3.10
14	0.0070	0.093	177.42	5.78	3.10

Table A2. Sensitivity analysis on K_{ts}.

K_{ts} [N/mm^2]	$a \cdot (r_{CE1})^4$ [mm^4]	$b \cdot (r_{CE1})^3$ [mm^4]	$c \cdot (r_{CE1})^2$ [mm^4]	$e \cdot (r_{CE1})$ [mm^4]	g [mm^4]
1	8.11×10^{-5}	-8.92×10^{-5}	-9.10×10^{-2}	5.01×10^{-2}	8.25×10^{-2}
10	8.11×10^{-5}	-8.94×10^{-6}	-9.85×10^{-2}	5.43×10^{-3}	9.67×10^{-2}
100	8.11×10^{-5}	-9.14×10^{-7}	-9.86×10^{-2}	5.56×10^{-4}	9.69×10^{-2}
1000	8.11×10^{-5}	-1.11×10^{-7}	-9.86×10^{-2}	6.77×10^{-5}	9.69×10^{-2}
10,000	8.11×10^{-5}	-3.11×10^{-8}	-9.86×10^{-2}	1.89×10^{-5}	9.69×10^{-2}
100,000	8.11×10^{-5}	-2.30×10^{-8}	-9.86×10^{-2}	1.40×10^{-5}	9.69×10^{-2}
1,000,000	8.11×10^{-5}	-2.22×10^{-8}	-9.86×10^{-2}	1.35×10^{-5}	9.69×10^{-2}

Table A3. Parameters of Equation (30) computed for each experimental test.

Test	fz [mm]	I [mm]	a [-]	b [mm]	c [mm^2]	e [mm^3]	g [mm^4]
1	0.0010	0.00000	0.00001	0.00000	-0.62252	0.00000	0.09688
2	0.0045	0.00007	0.00127	0.00000	-0.62252	0.00004	0.09688
3	0.0020	0.00002	0.00013	0.00000	-0.62252	0.00002	0.09688
4	0.0060	0.00003	0.00014	0.00000	-0.62252	0.00002	0.09688
5	0.0025	0.00003	0.00056	0.00000	-0.62252	0.00002	0.09688
6	0.0040	0.00008	0.00326	0.00000	-0.62252	0.00005	0.09688
7	0.0015	0.00001	0.00001	0.00000	-0.62252	0.00001	0.09688
8	0.0030	0.00008	0.00323	0.00000	-0.62252	0.00005	0.09688
9	0.0035	0.00006	0.00111	0.00000	-0.62252	0.00004	0.09688
10	0.0005	0.00001	0.00045	0.00000	-0.62252	0.00001	0.09688
11	0.0065	0.00002	0.00002	0.00000	-0.62252	0.00001	0.09688
12	0.0055	0.00014	0.00540	0.00000	-0.62252	0.00009	0.09688
13	0.0050	0.00007	0.00145	0.00000	-0.62252	0.00005	0.09688
14	0.0070	0.00012	0.00202	0.00000	-0.62252	0.00007	0.09688

References

1. Lewandowski, J.J.; Seifi, M. Metal Additive Manufacturing: A Review of Mechanical Properties. *Annu. Rev. Mater. Res.* **2016**, *46*, 151–186. [CrossRef]
2. Zhang, M.; Ye, X.; Li, Y.; Wang, H.; Lai, R.; Li, Y. Effect of Heat Treatment States of Feedstock on the Microstructure and Mechanical Properties of AA2219 Layers Deposited by Additive Friction Stir Deposition. *Materials* **2023**, *16*, 7591. [CrossRef]
3. Noga, P.; Skrzekut, T.; Wędrychowicz, M. Microstructure and Mechanical Properties of Al-Si Alloys Produced by Rapid Solidification and Hot Extrusion. *Materials* **2023**, *16*, 5223. [CrossRef] [PubMed]
4. Wu, H.; Rena, Y.; Rena, J.; Lianga, L.; Lia, R.; Fangb, Q.; Caic, A.; Shand, Q.; Tiane, Y.; Bakerf, I. Selective laser melted AlSi10Mg alloy under melting mode transition: Microstructure evolution, nanomechanical behaviors and tensile properties. *J. Alloys Compd.* **2021**, *873*, 159823. [CrossRef]
5. Wang, P.; Lei, H.; Zhu, X.; Chen, H.; Fang, D. Influence of manufacturing geometric defects on the mechanical properties of AlSi10Mg alloy fabricated by selective laser melting. *J. Alloys Compd.* **2019**, *789*, 852–859. [CrossRef]
6. Thijs, L.; Kempen, K.; Kruth, J.P.; Van Humbeeck, J. Fine-structured aluminium products with controllable texture by selective laser melting of pre-alloyed AlSi10Mg powder. *Acta Mater.* **2013**, *61*, 1809–1819. [CrossRef]
7. Chen, N.; Li, H.N.; Wu, J.; Li, Z.; Li, L.; Liu, G.; He, N. Advances in micro milling: From tool fabrication to process outcomes. *Int. J. Mach. Tools Manuf.* **2021**, *160*, 103670. [CrossRef]
8. Shivakoti, I.; Kibria, G.; Cep, R.; Pradhan, B.B.; Sharma, A. Laser Surface Texturing for Biomedical Applications: A Review. *Coatings* **2021**, *11*, 124. [CrossRef]
9. Pascu, S.; Balc, N. Process Parameter Optimization for Hybrid Manufacturing of PLA Components with Improved Surface Quality. *Polymers* **2023**, *15*, 3610. [CrossRef]
10. Cheng, K.; Huo, D. *Micro-Cutting: Fundamentals and Applications*; John Wiley & Sons: West Sussex, UK, 2013.
11. Joshy, J.; George, A.; Kuriachen, B.; Mathew, J. Influence of post processing on the micromachinability of selective laser melted AlSi10Mg: An experimental investigation. *Mater. Manuf. Process.* **2023**, *38*, 516–528. [CrossRef]
12. Pradhana, S.; Singha, S.; Prakasha, C.; Królczykb, G.; Pramanikc, A.; Pruncu, C.I. Investigation of machining characteristics of hard-to-machine Ti-6Al-4V-ELI alloy for biomedical applications. *J. Mater. Res. Technol.* **2019**, *8*, 4849–4862. [CrossRef]
13. Cardoso, P.; Davim, J.P. Optimization of Surface Roughness in Micromilling. *Mater. Manuf. Process.* **2010**, *25*, 1115–1119. [CrossRef]
14. Shi, Z.; Liu, Z.; Li, Y.; Qiao, Y. Swept Mechanism of Micro-Milling Tool Geometry Effect on Machined Oxygen Free High Conductivity Copper (OFHC) Surface Roughness. *Materials* **2017**, *10*, 120. [CrossRef]
15. Dhanorker, A.; Özel, T. Meso/micro scale milling for micro-manufacturing. *Int. J. Mechatron. Manuf. Syst.* **2008**, *1*, 23. [CrossRef]

16. Balázs, B.Z.; Geier, N.; Takács, M.; Davim, J.P. A review on micro-milling: Recent advances and future trends. *Int. J. Adv. Manuf. Technol.* **2021**, *112*, 655–684. [CrossRef]

17. Xie, M.; Yu, X.; Bao, W.; Liu, C.; Xia, M. Side-Milling-Force Model Considering Tool Runout and Workpiece Deformation. *Electronics* **2023**, *12*, 968. [CrossRef]

18. Lu, X.; Cong, C.; Hou, P.; Xv, K.; Liang, S.Y. Improved Cutting Force Modelling in Micro-Milling Aluminum Alloy LF 21 Considering Tool Wear. *Appl. Sci.* **2022**, *12*, 5357. [CrossRef]

19. Cappellini, C.; Malandruccolo, A.; Abeni, A.; Attanasio, A. A feasibility study of promoting osseointegration surface roughness by micro-milling of Ti-6Al-4V biomedical alloy. *Int. J. Adv. Manuf. Technol.* **2023**, *126*, 3053–3067. [CrossRef]

20. Żurawski, K.; Żurek, P.; Kawalec, A.; Bazan, A.; Olko, A. Modeling of Surface Topography after Milling with a Lens-Shaped End-Mill, Considering Runout. *Materials* **2022**, *15*, 1188. [CrossRef]

21. Attanasio, A. Tool Run-Out Measurement in Micro Milling. *Micromachines* **2017**, *8*, 221. [CrossRef]

22. Krüger, M.; Denkena, B. Model-based identification of tool runout in end milling and estimation of surface roughness from measured cutting forces. *Int. J. Adv. Manuf. Technol.* **2012**, *65*, 1067–1080. [CrossRef]

23. Diez, E.; Perez, H.; Guzman, M.; Vizan, A. An improved methodology for the experimental evaluation of tool runout in peripheral milling. *Int. J. Adv. Manuf. Technol.* **2013**, *65*, 283–293. [CrossRef]

24. Abeni, A.; Loda, D.; Özel, T.; Attanasio, A. Analytical force modelling for micro milling additively fabricated Inconel 625. *Prod. Eng.* **2020**, *4*, 613–627. [CrossRef]

25. Chen, W.; Teng, X.; Huo, D.; Wang, Q. An improved cutting force model for micro milling considering machining dynamics. *Int. J. Adv. Manuf. Technol.* **2017**, *93*, 3005–3016. [CrossRef]

26. Cappellini, C.; Abeni, A.; Attanasio, A. Modelling of micro-milling by considering tool run-out and ploughing regime. *Proc. CIRP* **2023**, *118*, 402–407. [CrossRef]

27. Singh, K.; Kartik, V.; Singh, R. Stability modeling with dynamic run-out in high speed micromilling of Ti6Al4V. *Int. J. Mech. Sci.* **2019**, *150*, 677–690. [CrossRef]

28. Jing, X.; Lv, R.; Song, B.; Xu, J.; Jaffery, S.H.I.; Li, H. A novel run-out model based on spatial tool position for micro-milling force prediction. *J. Manuf. Process.* **2021**, *68*, 739–749. [CrossRef]

29. Chen, Y.; Lu, J.; Deng, Q.; Ma, J.; Liao, X. Modeling study of milling force considering tool runout at different types of radial cutting depth. *J. Manuf. Process.* **2022**, *76*, 486–503. [CrossRef]

30. Vogler, M.P.; Kapoor, S.G.; DeVor, R.E. On the modeling and analysis of machining per- formance in micro end milling, part II: Cutting force prediction. *ASME J. Manuf. Sci. Eng.* **2004**, *126*, 695–705. [CrossRef]

31. Zhang, X.; Yu, T.; Wang, W. Cutting forces modeling for micro flat end milling by considering tool run-out and bottom edge cutting effect. *Proc. Inst. Mech. Eng. Part. B J. Eng. Manuf.* **2017**, *233*, 470–485. [CrossRef]

32. Wan, M.; Zhang, W.H.; Dang, J.W.; Yang, Y. New procedures for calibration of instantaneous cutting force coefficients and cutter runout parameters in peripheral milling. *Int. J. Mach. Tools Manuf.* **2009**, *49*, 1144–1151. [CrossRef]

33. Sun, Z.; Geng, D.; Meng, F.; Zhou, L.; Jiang, X.; Zhang, D. High performance drilling of T800 CFRP composites by combining ultrasonic vibration and optimized drill structure. *Ultrasonics* **2023**, *134*, 107097. [CrossRef]

34. Sun, Z.; Geng, D.; Guo, H.; Zhang, Q.; Liu, Y.; Liu, L.; Jiang, X.; Zhang, D. Introducing transversal vibration in twist drilling: Material removal mechanisms and surface integrity. *J. Mater. Process Technol.* **2024**, *325*, 118296. [CrossRef]

35. Abeni, A.; Lancini, M. and Attanasio, A. Characterization of machine tools and measurement system for micromilling. *Nanotechnol. Precis. Eng.* **2019**, *2*, 23–28. [CrossRef]